INTERNATIONAL JOURNAL FOR NUMERICAL METHODS IN FLUIDS
Int. J. Numer. Meth. Fluids 2010; **62**:683–708
Published online 23 March 2009 in Wiley InterScience (www.interscience.wiley.com). DOI: 10.1002/fld.2039

A transformation-free HOC scheme for incompressible viscous flows on nonuniform polar grids

Rajendra K. Ray*,† and Jiten C. Kalita‡

Department of Mathematics, Indian Institute of Technology, Guwahati 781039, India

SUMMARY

We recently proposed a transformation-free higher-order compact (HOC) scheme for two-dimensional (2-D) steady convection–diffusion equations on nonuniform Cartesian grids (*Int. J. Numer. Meth. Fluids* 2004; **44**:33–53). As the scheme was equipped to handle only constant coefficients for the second-order derivatives, it could not be extended directly to curvilinear coordinates, where they invariably occur as variables.

In this paper, we extend the scheme to cylindrical polar coordinates for the 2-D convection–diffusion equations and more specifically to the 2-D incompressible viscous flows governed by the Navier–Stokes (N–S) equations. We first apply the formulation to a problem having analytical solution and demonstrate its fourth-order spatial accuracy. We then apply it to the flow past an impulsively started circular cylinder problem and finally to the driven polar cavity problem. We present our numerical results and compare them with established numerical and analytical and experimental results whenever available. This new approach is seen to produce excellent comparison in all the cases.

Received 26 May 2008; Revised 7 February 2009; Accepted 9 February 2009

KEY WORDS: HOC; convection–diffusion; nonuniform; N–S equations; circular cylinder; polar cavity

1. INTRODUCTION

The steady two-dimensional (2-D) convection–diffusion equation in Cartesian coordinate system (x, y) for a transport variable ϕ in some continuous domain with suitable boundary conditions can be written as

$$-\nabla^2\phi + c_1(x, y)\frac{\partial\phi}{\partial x} + c_2(x, y)\frac{\partial\phi}{\partial y} = f(x, y) \tag{1}$$

*Correspondence to: Rajendra K. Ray, Department of Mathematics, Indian Institute of Technology, Guwahati 781039, India.
†E-mail: rkr@iitg.ernet.in
‡Associate Professor.

c_1 and c_2 are the convection coefficients, and f is a forcing function. In Equation (1), the magnitude of the convection coefficients determines the ratio of convection to diffusion and is sometimes referred to as the Reynolds number (Re). The equation becomes convection dominated for large Re's and diffusion dominated for small Re's. Most of the steady 2-D flows are expressed in this form. It represents the convection–diffusion of many fluid variables such as mass, heat, energy, vorticity, etc. With proper choice of c_1, c_2 and f, it can also be used to represent the complete Navier–Stokes (N–S) equations.

The higher-order compact (HOC) finite difference schemes for the computation of incompressible viscous flows [1–15] are gradually gaining popularity because of their high accuracy and advantages associated with compact difference stencils. Most of these schemes were developed for equations of the convection–diffusion type (1) and were well equipped to simulate incompressible viscous flows governed by the N–S equations as well. A compact finite difference scheme is one that utilizes grid points located only directly adjacent to the node about which the differences are taken. In addition, if the scheme has an order of accuracy greater than two, it is termed an HOC method. The higher-order accuracy of the HOC methods combined with the compactness of the difference stencils yields highly accurate numerical solutions on relatively coarser grids with greater computational efficiency. However, most of the HOC schemes developed so far are mostly on uniform grids [1, 3–7, 9–12, 15]. The very few attempts that have been made to develop HOC scheme on nonuniform grids for the convection–diffusion equations [12–14, 16, 17] use the conventional transformation technique from the physical plane to the computational plane. The solution is then computed on a rectangular uniform grid on the computational plane and eventually transformed back to the physical plane. This inevitably brings in the complications of having to deal with some new cross-derivative terms in the transformed partial differential equations (PDE) along with increase in arithmetic operations. In addition, the advantage of setting the diffusion coefficients appearing in the PDEs in the physical space to unity is lost because they no longer remain the same in the transformed space.

In a departure from this practice, Kalita *et al.* [2] developed an HOC scheme on rectangular nonuniform grids for the steady 2-D convection–diffusion equation with variable coefficients without any transformation. It was based on the Taylor series expansion of a continuous function at a particular point for two different step lengths and approximation of the derivatives appearing in the 2-D convection–diffusion equation on a nonuniform stencil. The original PDE was then used again to replace the derivative terms appearing in the finite difference approximations, resulting in a higher-order scheme on a compact stencil of nine points.

However, direct implementation of this and other approaches [1, 3, 4, 7, 9–12, 15] on polar coordinates was not possible because of the fact that the second-order partial derivatives of the transport variable representing the phenomenon of diffusion invariably come with variable coefficients. All these schemes were equipped to deal with the variable convection coefficients only. In polar coordinate system (r, θ), Equation (1) takes the form

$$-\nabla^2\phi + c_1(r,\theta)\frac{\partial\phi}{\partial r} + c_2(r,\theta)\frac{\partial\phi}{\partial\theta} = f(r,\theta) \tag{2}$$

Though Equations (1) and (2) are identical, the Laplacians appearing in the two equations are different in terms of coefficients of the second-order partial derivatives with respect to the

DOI: 10.1002/fld

independent variables. Assorting derivatives of different orders, (2) may be written as

$$-\frac{\partial^2\phi}{\partial r^2}-\frac{1}{r^2}\frac{\partial^2\phi}{\partial\theta^2}+\left(c_1(r,\theta)-\frac{1}{r}\right)\frac{\partial\phi}{\partial r}+c_2(r,\theta)\frac{\partial\phi}{\partial\theta}=f(r,\theta) \tag{3}$$

In this paper, we extend the philosophy outlined in Reference [2] to develop an HOC scheme for 2-D convection–diffusion equations on cylindrical polar coordinates. This is accomplished by considering the coefficients of all the partial derivatives appearing in Equation (3) as variables, thus making way for a straightforward extension of the proposed formulation to orthogonal curvilinear coordinate system as well. It may be mentioned that the majority of the earlier endeavors to develop HOC schemes on cylindrical polar coordinates were confined to the Poisson equation on uniform grids [3, 15, 18–24].

To validate the proposed scheme, we first apply it to a problem of pure diffusion in polar coordinates with known analytical solution and also carry out error analysis. In the process, we also establish the theoretical rate of convergence of the scheme. The robustness of the scheme, however, is better realized when it is applied to the problems of flow past an impulsively started circular cylinder and the driven polar cavity. Both these flows are governed by the steady-state incompressible N–S equations. We have used the streamfunction–vorticity (ψ–ω) formulation of the N–S equations for computing the flows. For the pure diffusion problem, our numerical results are extremely close to the analytical results, whereas for the cylinder and cavity problems, our solution agrees very well, both qualitatively and quantitatively with established numerical and experimental results. The scheme is also seen to handle both Dirichlet (in the first problem) and Neumann boundary conditions with ease (in the other two).

The paper has been arranged in five sections. Section 2 deals with the mathematical formulation and discretization, Section 3 with the solution of the algebraic system of equations, Section 4 with the numerical test cases and finally, Section 5 summarizes the whole work.

2. MATHEMATICAL FORMULATIONS AND DISCRETIZATION PROCEDURES

A more generalized form of Equation (3) in an annular region $[r_1, r_2]\times[\theta_1, \theta_2]$ may be written as

$$a(r,\theta)\frac{\partial^2\phi}{\partial r^2}+b(r,\theta)\frac{\partial^2\phi}{\partial\theta^2}+c(r,\theta)\frac{\partial\phi}{\partial r}+d(r,\theta)\frac{\partial\phi}{\partial\theta}=f(r,\theta) \tag{4}$$

Constructing on it, a nonuniform polar mesh (see a typical stencil in Figure 1), the HOC approximations for the first and second derivatives appearing in (4) at the (i, j)th node [2] can be obtained as follows:

$$\left.\frac{\partial\phi}{\partial r}\right|_{i,j}=\delta_r\phi_{i,j}-\frac{1}{2}(r_f-r_b)\delta_r^2\phi_{i,j}-\frac{r_f r_b}{6}\left.\frac{\partial^3\phi}{\partial r^3}\right|_{i,j}-\frac{1}{24}r_f r_b(r_f-r_b)\left.\frac{\partial^4\phi}{\partial r^4}\right|_{i,j}+O\left(\frac{r_f^5+r_b^5}{r_f+r_b}\right) \tag{5}$$

DOI: 10.1002/fld

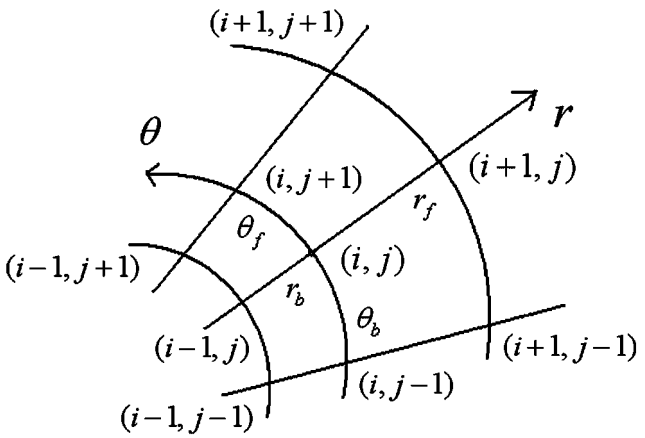

Figure 1. The nonuniform HOC stencil on polar coordinates.

$$\left.\frac{\partial^2\phi}{\partial r^2}\right|_{i,j} = \delta_r^2\phi_{i,j} - \frac{1}{3}(r_f - r_b)\left.\frac{\partial^3\phi}{\partial r^3}\right|_{i,j} - \frac{1}{12}(r_f^2 + r_b^2 - r_f r_b)\left.\frac{\partial^4\phi}{\partial r^4}\right|_{i,j} - \frac{1}{60}(r_f - r_b)(r_f^2 + r_b^2)\left.\frac{\partial^5\phi}{\partial r^5}\right|_{i,j} + O\left(\frac{r_f^5 + r_b^5}{r_f + r_b}\right) \tag{6}$$

The derivatives with respect to θ can be obtained in a similar way; here, $r_f = (r_{i+1} - r_i)$, $r_b = (r_i - r_{i-1})$ and $\theta_f = (\theta_{j+1} - \theta_j)$, $\theta_b = (\theta_j - \theta_{j-1})$. The details of the nonuniform central difference operators δ_r, δ_r^2, δ_θ and δ_θ^2 can be found in the Appendix. In view of the above equations, Equation (4) may be approximated at the point (i, j) as

$$[a\delta_r^2 + b\delta_\theta^2 + c\{\delta_r - 0.5(r_f - r_b)\delta_r^2\} + d\{\delta_\theta - 0.5(\theta_f - \theta_b)\delta_\theta^2\}]\phi_{i,j} + \tau_{i,j} = f_{i,j} \tag{7}$$

where $\tau_{i,j}$ is the truncation error given by

$$\tau_{i,j} = -H_1\frac{\partial^3\phi}{\partial r^3} - K_1\frac{\partial^3\phi}{\partial\theta^3} - H_2\frac{\partial^4\phi}{\partial r^4} - K_2\frac{\partial^4\phi}{\partial\theta^4} + (r_f - r_b)(r_f^2 + r_b^2)\phi_1 + (\theta_f - \theta_b)(\theta_f^2 + \theta_b^2)\phi_2 + O\left(\frac{r_f^5 + r_b^5}{r_f + r_b}, \frac{\theta_f^5 + \theta_b^5}{\theta_f + \theta_b}\right) \tag{8}$$

with ϕ_1, ϕ_2 being the leading truncation error terms and

$$H_1 = \tfrac{1}{6}\{2a(r_f - r_b) + cr_f r_b\}, \quad H_2 = \tfrac{1}{24}\{2a(r_f^2 + r_b^2 - r_f r_b) + cr_f r_b(r_f - r_b)\}$$

$$K_1 = \tfrac{1}{6}\{2b(\theta_f - \theta_b) + \mathrm{d}\theta_f\theta_b\}, \quad K_2 = \tfrac{1}{24}\{2b(\theta_f^2 + \theta_b^2 - \theta_f\theta_b) + \mathrm{d}\theta_f\theta_b(\theta_f - \theta_b)\}$$

DOI: 10.1002/fld

Successive differentiation of (4) with respect to r and rearranging terms yield

$$\frac{\partial^3\phi}{\partial r^3}=-\frac{1}{a}\{(a_r+c)\delta_r^2\phi+c_r\delta_r\phi+\mathrm{d}\delta_r\delta_\theta\phi+b\delta_r\delta_\theta^2\phi+\mathrm{d}_r\delta_\theta\phi+b_r\delta_\theta^2\phi-f_r\} \tag{9}$$

$$\frac{\partial^4\phi}{\partial r^4}=L_1\delta_r^2\phi+L_2\delta_r\phi+L_3\delta_r\delta_\theta\phi+L_4\delta_r\delta_\theta^2\phi-\frac{d}{a}\delta_r^2\delta_\theta\phi-\frac{b}{a}\delta_r^2\delta_\theta^2\phi+L_5\delta_\theta\phi+L_6\delta_\theta^2\phi$$
$$-\frac{1}{a^2}(2a_r+c)f_r+\frac{1}{a}f_{rr} \tag{10}$$

with

$$L_1=\frac{1}{a^2}(2a_r^2+3ca_r+c^2)-\frac{1}{a}(a_{rr}+2c_r),\quad L_2=\frac{c_r}{a^2}(2a_r+c)-\frac{c_{rr}}{a}$$
$$L_3=\frac{d}{a^2}(2a_r+c)-\frac{2d_r}{a},\quad L_4=\frac{b}{a^2}(2a_r+c)-\frac{2b_r}{a}$$
$$L_5=\frac{d_r}{a^2}(2a_r+c)-\frac{d_{rr}}{a},\quad L_6=\frac{b_r}{a^2}(2a_r+c)-\frac{b_{rr}}{a}$$

Likewise

$$\frac{\partial^3\phi}{\partial\theta^3}=-\frac{1}{b}\{(b_\theta+d)\delta_\theta^2\phi+d_\theta\delta_\theta\phi+c\delta_r\delta_\theta\phi+a\delta_r^2\delta_\theta\phi+c_\theta\delta_r\phi+a_\theta\delta_r^2\phi-f_\theta\} \tag{11}$$

$$\frac{\partial^4\phi}{\partial\theta^4}=\left\{\frac{1}{b^2}(2b_\theta^2+3db_\theta+d^2)-\frac{1}{b}(b_{\theta\theta}+2d_\theta)\right\}\delta_\theta^2\phi+\left\{\frac{d_\theta}{b^2}(2b_\theta+d)-\frac{c_{\theta\theta}}{b}\right\}\delta_\theta\phi$$
$$+\left\{\frac{c}{b^2}(2b_\theta+d)-\frac{2c_\theta}{b}\right\}\delta_r\delta_\theta\phi+\left\{\frac{a}{b^2}(2b_\theta+d)-\frac{2a_\theta}{b}\right\}\delta_r^2\delta_\theta\phi-\frac{a}{b}\delta_r^2\delta_\theta^2\phi-\frac{c}{b}\delta_r\delta_\theta^2\phi$$
$$+\left\{\frac{c_\theta}{b^2}(2b_\theta+d)-\frac{c_{\theta\theta}}{b}\right\}\delta_r\phi+\left\{\frac{a_\theta}{b^2}(2b_\theta+d)-\frac{a_{\theta\theta}}{b}\right\}\delta_r^2\phi$$
$$-\frac{1}{b^2}(2b_\theta+d)f_\theta+\frac{1}{b}f_{\theta\theta} \tag{12}$$

Using (9)–(12), Equation (8) can be written as

$$\tau_{i,j}=[E1_{i,j}\delta_r^2+E2_{i,j}\delta_\theta^2+E3_{i,j}\delta_r+E4_{i,j}\delta_\theta+E5_{i,j}\delta_r\delta_\theta$$
$$+E6_{i,j}\delta_r\delta_\theta^2+E7_{i,j}\delta_r^2\delta_\theta+E8_{i,j}\delta_r^2\delta_\theta^2]\phi_{i,j}-F1_{i,j} \tag{13}$$

where

$$E1_{i,j}=\frac{(a_r+c)}{a}\left\{H_1-\frac{H_2}{a}(2a_r+c)\right\}+\frac{H_2}{a}(a_{rr}+2c_r)+\frac{a_\theta}{b}\left\{K_1-\frac{K_2}{b}(2b_\theta+d)\right\}+\frac{K_2a_{\theta\theta}}{b}$$

$$E2_{i,j}=\frac{b_r}{a}\left\{H_1-\frac{H_2}{a}(2a_r+c)\right\}+\frac{H_2b_{rr}}{a}+\frac{(b_\theta+d)}{b}\left\{K_1-\frac{K_2}{b}(2b_\theta+d)\right\}+\frac{K_2}{b}(b_{\theta\theta}+2d_\theta)$$

DOI: 10.1002/fld

$$E3_{i,j}=\frac{c_r}{a}\left\{H_1-\frac{H_2}{a}(2a_r+c)\right\}+\frac{H_2c_{rr}}{a}+\frac{c_\theta}{b}\left\{K_1-\frac{K_2}{b}(2b_\theta+d)\right\}+\frac{K_2c_{\theta\theta}}{b}$$

$$E4_{i,j}=\frac{d_r}{a}\left\{H_1-\frac{H_2}{a}(2a_r+c)\right\}+\frac{H_2d_{rr}}{a}+\frac{d_\theta}{b}\left\{K_1-\frac{K_2}{b}(2b_\theta+d)\right\}+\frac{K_2c_{\theta\theta}}{b}$$

$$E5_{i,j}=\frac{d}{a}\left\{H_1-\frac{H_2}{a}(2a_r+c)\right\}+\frac{2H_2d_r}{a}+\frac{c}{b}\left\{K_1-\frac{K_2}{b}(2b_\theta+d)\right\}+\frac{2K_2c_\theta}{b}$$

$$E6_{i,j}=\frac{b}{a}\left\{H_1-\frac{H_2}{a}(2a_r+c)\right\}+\frac{2H_2b_r}{a}+\frac{K_2c}{b}$$

$$E7_{i,j}=\frac{H_2d}{a}+\frac{a}{b}\left\{K_1-\frac{K_2}{b}(2b_\theta+d)\right\}+\frac{2K_2a_\theta}{b}$$

$$E8_{i,j}=\frac{bH_2}{a}+\frac{aK_2}{b}$$

$$F1_{i,j}=\left[\frac{1}{a}\left\{H_1-\frac{H_2}{a}(2a_r+c)\right\}\delta_r+\frac{H_2}{a}\delta_r^2+\frac{1}{b}\left\{K_1-\frac{K_2}{b}(2b_\theta+d)\right\}\delta_\theta+\frac{K_2}{b}\delta_\theta^2\right]f_{i,j}$$

Substituting (13) in (7), the HOC approximation of Equation (4) on nonuniform polar grids can be written as

$$[A_{i,j}\delta_r^2+B_{i,j}\delta_\theta^2+C_{i,j}\delta_r+D_{i,j}\delta_\theta+G_{i,j}\delta_r\delta_\theta+H_{i,j}\delta_r\delta_\theta^2+K_{i,j}\delta_r^2\delta_\theta+L_{i,j}\delta_r^2\delta_\theta^2]\phi_{i,j}=F_{i,j} \quad (14)$$

where the coefficients are given by

$$A_{i,j}=a_{i,j}+E1_{i,j}-0.5(r_f-r_b)c_{i,j}$$

$$B_{i,j}=b_{i,j}+E2_{i,j}-0.5(\theta_f-\theta_b)d_{i,j}$$

$$C_{i,j}=c_{i,j}+E3_{i,j},\quad D_{i,j}=d_{i,j}+E4_{i,j},\quad G_{i,j}=E5_{i,j}$$

$$H_{i,j}=E6_{i,j},\quad K_{i,j}=E7_{i,j},\quad L_{i,j}=E8_{i,j},\quad F_{i,j}=f_{i,j}+F1_{i,j}$$

If (r,θ) is replaced by (u_1,u_2), where u_1 and u_2 are the coordinate curves of an orthogonal curvilinear coordinate system, (14) also represents the HOC scheme on nonuniform grids for Equation (4) in curvilinear coordinate system (u_1,u_2). Thus, the extension of the current scheme from polar coordinates to general orthogonal curvilinear coordinate system in 2-D is a mere formality.

It is important to note that while simulating flows on curvilinear geometries by solving equations of the form (4), one may come across the terms of the form $\frac{0}{0}$. In such cases, one may resolve the $\frac{0}{0}$ form by using the L'Hospital rule whenever possible or employ a local Cartesian mesh at the point of singularity [25]. Other strategies for handling such singularities can be found in References [18, 24, 26].

DOI: 10.1002/fld

3. SOLUTION OF ALGEBRAIC SYSTEMS

We now discuss the solution of algebraic systems associated with the newly proposed finite difference approximations. The system of equations (14) can be written as

$$\sum_{k_1=-1}^{1}\sum_{k_2=-1}^{1}\eta_{i+k_1,j+k_2}\phi_{i+k_1,j+k_2}=\sum_{k_1=-1}^{1}\sum_{k_2=-1}^{1}\xi_{i+k_1,j+k_2}f_{i+k_1,j+k_2} \tag{15}$$

where η, ξ's are functions of the coefficients a, b, c and d appearing in Equation (4), their derivatives and the step lengths r_f, r_b, θ_f and θ_b. In matrix form, the system of algebraic equations given by (15) can now be written as

$$A\Phi = F \tag{16}$$

where the coefficient matrix A is an asymmetric sparse matrix with each row containing at most nine nonzero entries. For a grid of size $m \times n$, A is of size $mn \times mn$, and Φ and F are mn-component vectors.

The next step now is to solve Equation (16); as the coefficient matrix A is not generally diagonally dominant, conventional solvers such as Gauss–Seidel cannot be used. On uniform grids in Cartesian coordinates, some of the associated matrices are symmetric and positive definite, which allows algorithms like conjugate-gradient (CG) [27, 28] to be used. As the nonuniform grid and variable coefficients a, b, c and d of Equation (4) invariably lead to nonsymmetric matrices, in order to solve these systems, we use the hybrid biconjugate gradient stabilized method BiCGStab(2) [27, 28] without preconditioning.

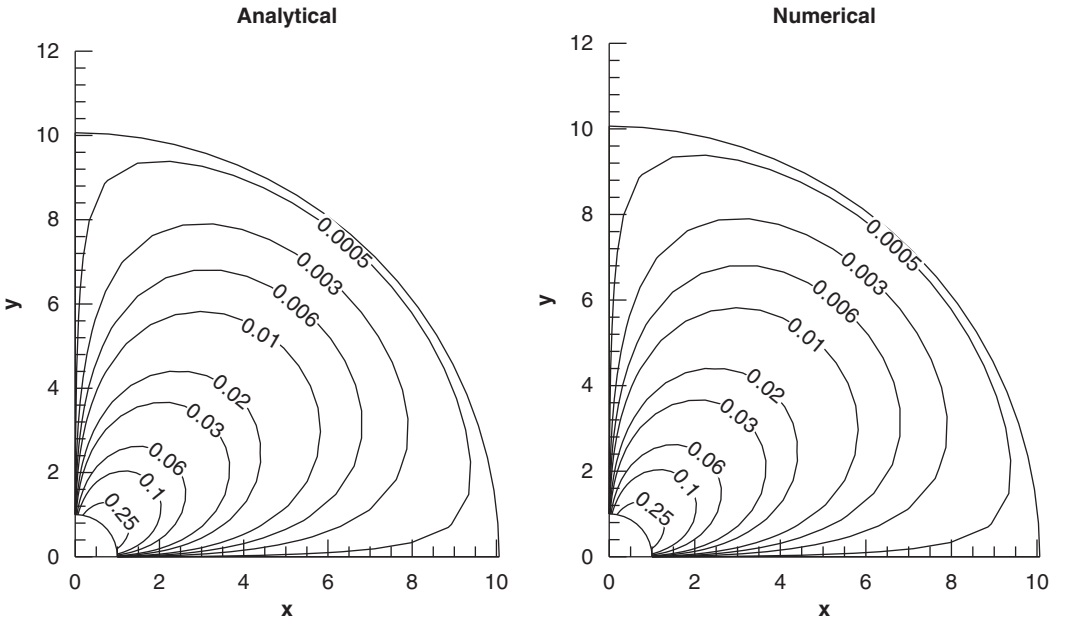

Figure 2. Contours of the analytical and numerical solutions on a 21×21 grid for Problem 1.

DOI: 10.1002/fld

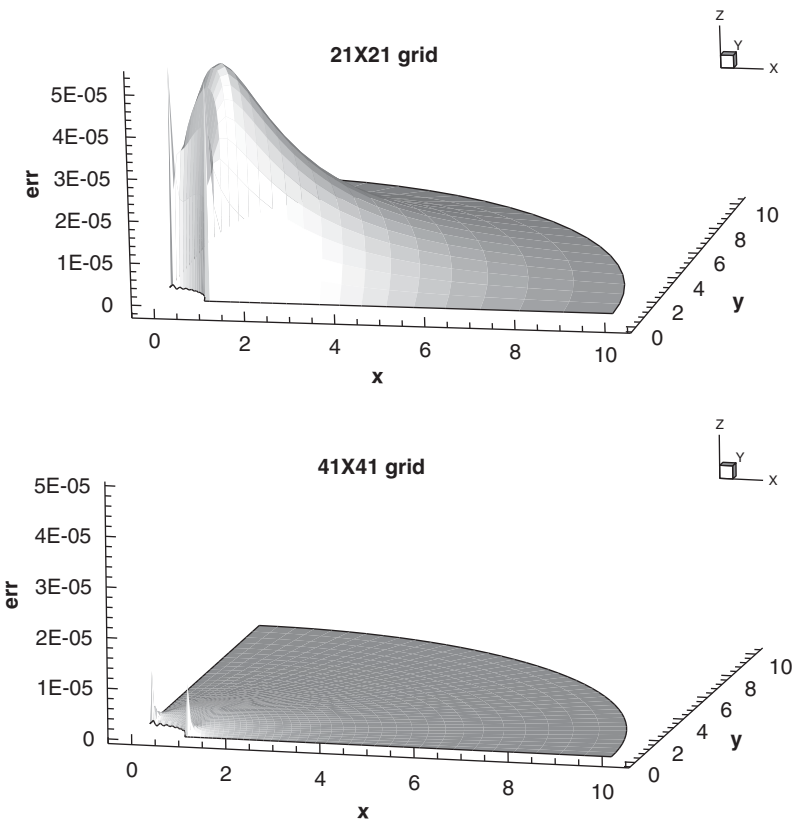

Figure 3. Surface plots of errors on 21×21 (top) and 41×41 (bottom) grids for Problem 1.

It may be noted that for the coupled nonlinear PDEs (such as the ψ–ω form of the N–S equations), an iterative solution procedure must be adopted. These iterations may be termed as outer iterations. We use a decoupled algorithm where vorticity and stream functions are solved iteratively and sequentially through hybrid BiCGStab(2) and lagging the appropriate terms. The latter iterations may be termed as inner iterations, which must be carried out at every outer iteration with updated data. We utilize a relaxation parameter γ for the inner iteration cycles for both ω and ψ. In general, for larger values of Reynolds number, we needed smaller values of γ.

All of our computations were carried out on a Pentium 4 based PC with 512 MB RAM. For the inner iterations, the computations were stopped when the norm of the residual vector $\bar{\mathbf{r}} = F - A\Phi$ (ϕ being either ω or ψ) arising out of Equation (16) fell below 0.5×10^{-6}. For the steady-state solution of the problems governed by the N–S equations, steady state was assumed to reach when the maximum ω-error between two successive outer iteration steps was smaller than 1.0×10^{-9}.

4. NUMERICAL EXPERIMENTS

In order to study the validity and effectiveness of the proposed scheme, it is applied to three problems. These are (i) a problem of pure diffusion, (ii) the flow past an impulsively started

DOI: 10.1002/fld

Table I. Problem 1: rate of convergence at selected grid points.

Grid size	Location	Computed solution	Analytical solution	Abs. error	Convergence rate
21×21		1.973200e−1		5.252619e−5	
					4.0070
41×41	(1.781165, 0.863938)	1.973692e−1	1.973725e−1	3.267036e−6	
					4.0017
81×81		1.973723e−1		2.039531e−7	
					3.9993
161×161		1.973725e−1		1.275361e−8	
21×21		2.270335e−1		4.072842e−5	
					4.0085
41×41	(1.413912, 0.392699)	2.270717e−1	2.270742e−1	2.530637e−6	
					4.0021
81×81		2.270741e−1		1.579332e−7	
					4.0000
161×161		2.270742e−1		9.871125e−9	
21×21		6.007732e−3		5.516783e−6	
					4.0046
41×41	(7.989783, 0.785398)	6.012905e−3	6.013249e−3	3.437078e−7	
					3.9966
81×81		6.013227e−3		2.153169e−8	
					3.8526
161×161		6.013247e−3		1.490525e−9	
21×21		6.257496e−2		3.414488e−5	
					4.0069
41×41	(3.172549, 0.785398)	6.260698e−2	6.260911e−2	2.123918e−6	
					4.0014
81×81		6.260898e−2		1.326146e−7	
					3.9947
161×161		6.260910e−2		8.319174e−9	

circular cylinder and (iii) the driven polar cavity flow problem. As the first problem has analytical solutions, Dirichlet boundary conditions are used, while for the next two, both Dirichlet (for ψ) and Neumann (for ω) boundary conditions are applied.

4.1. Test problem 1: a problem of pure diffusion

We consider the equation

$$\frac{\partial^2\phi}{\partial r^2}+\frac{1}{r}\frac{\partial\phi}{\partial r}+\frac{1}{r^2}\frac{\partial^2\phi}{\partial\theta^2}=0 \tag{17}$$

in the region $[\alpha,\beta]\times[0,\pi/2]$, with the boundary conditions

$$\phi(\alpha,\theta)=\theta\left(\frac{\pi}{2}-\theta\right)\quad\text{and}\quad\phi(\beta,\theta)=0\quad\text{for } 0\leqslant\theta\leqslant\pi/2$$

$$\phi(r,0)=\phi\left(r,\frac{\pi}{2}\right)=0\quad\text{for } \alpha\leqslant r\leqslant\beta$$

DOI: 10.1002/fld

The analytical solution of (17) is given by

$$\phi(r,\theta)=\sum_{n=1}^{\infty}\frac{2}{\pi}\frac{1}{(2n-1)^3}\left(\frac{\alpha}{r}\right)^{(4n-2)}\sin(4n-2)\theta\left(\frac{r^{(8n-4)}-\beta^{(8n-4)}}{\alpha^{(8n-4)}-\beta^{(8n-4)}}\right) \tag{18}$$

We present our results computed on grid sizes ranging from 21×21 to 161×161 for $\alpha=1$ and $\beta=10$ in Figures 2 and 3 and Table I. Figure 2 displays the analytical and numerical contours of the solution. It is heartening to note that on a grid of size 21×21 only, one can hardly distinguish the numerical solutions from the exact ones. This fact is also confirmed by Figure 3, where the surface plots of the errors are shown on two different grid sizes 21×21 and 41×41 for which the maximum absolute errors are extremely small, namely 5.29×10^{-5} and 1.03×10^{-5} only.

In Table I, we exhibit the analytical and computed solutions at four representative points on the solution domain along with the absolute errors on four different grid sizes. It is seen from the table that with grid refinement, the point-wise error decays with $O(h^4)$, as expected. Here, the rate of convergence is calculated as

$$M=\frac{\log(e_1/e_2)}{\log(N_2/N_1)}$$

where e_1, e_2 are the absolute errors estimated at a particular point for two different grids with N_1+1 and N_2+1 points in the either direction. It may be noted that the maximum errors for different grids occur at different points and are not directly comparable.

4.2. Test problem 2: flow past an impulsively started circular cylinder

Next we consider the steady, incompressible flow over an infinitely long cylinder of circular cross-section. The flow is governed by the incompressible N–S equations. We use the ψ–ω formulation of the N–S equations in cylindrical polar coordinates (r,θ). In nondimensional form, they are given by

$$\frac{\partial^2\omega}{\partial r^2}+\frac{1}{r}\frac{\partial\omega}{\partial r}+\frac{1}{r^2}\frac{\partial^2\omega}{\partial\theta^2}=Re\left(u\frac{\partial\omega}{\partial r}+\frac{v}{r}\frac{\partial\omega}{\partial\theta}\right) \tag{19}$$

$$\frac{\partial^2\psi}{\partial r^2}+\frac{1}{r}\frac{\partial\psi}{\partial r}+\frac{1}{r^2}\frac{\partial^2\psi}{\partial\theta^2}=-\omega \tag{20}$$

Here, ψ is the streamfunction, ω the vorticity, u, v, respectively, are the radial and tangential velocity components and $Re=UD/v$ is the Reynolds number with U being the characteristic velocity, D the diameter of the cylinder and v the kinematic viscosity. The velocities u and v in terms of ψ are given by

$$u=\frac{1}{r}\frac{\partial\psi}{\partial\theta}\quad\text{and}\quad v=-\frac{\partial\psi}{\partial r} \tag{21}$$

and the vorticity ω is given by

$$\omega=\frac{1}{r}\left[\frac{\partial}{\partial r}(vr)-\frac{\partial u}{\partial\theta}\right] \tag{22}$$

DOI: 10.1002/fld

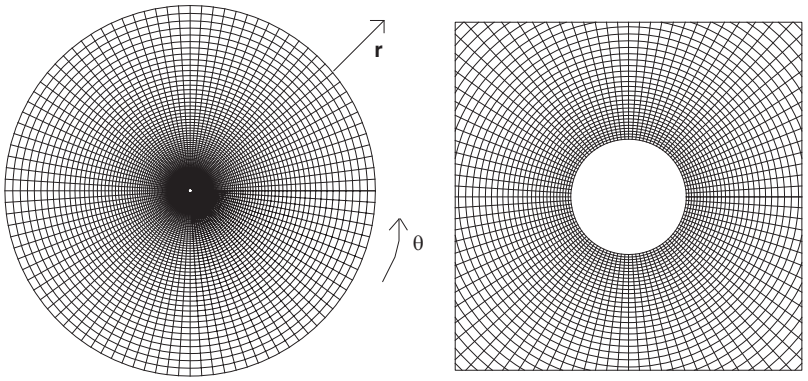

Figure 4. A typical 101×101 mesh for the flow past a circular cylinder problem.

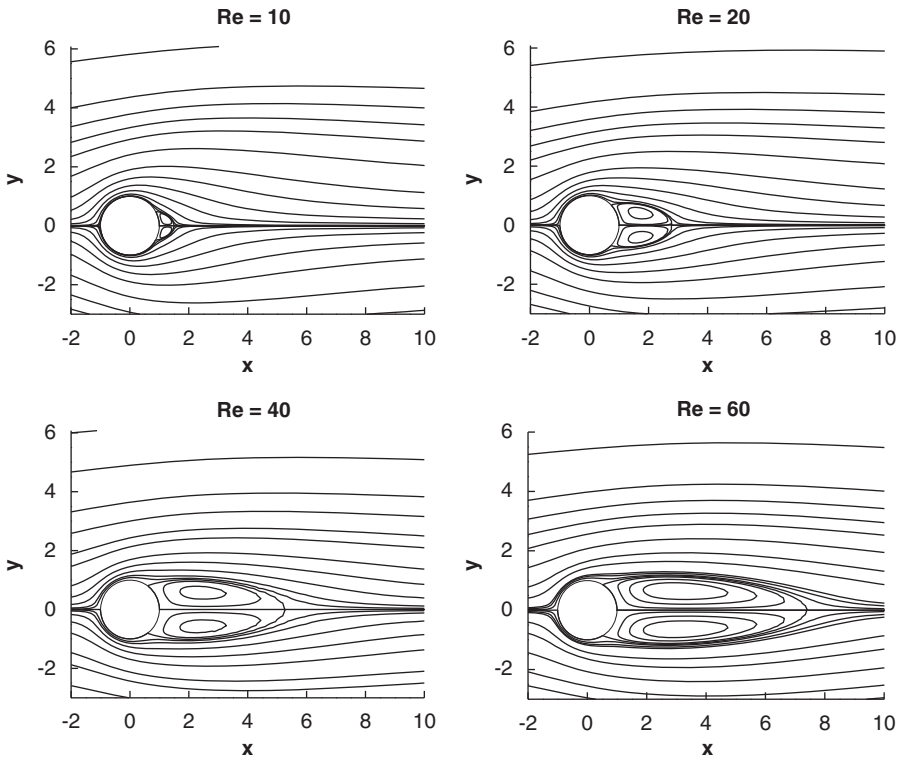

Figure 5. Steady-state streamlines for $Re = 10, 20, 40$ and 60 for the motion past a circular cylinder problem.

We assume the cylinder to be of unit radius placed in an infinite domain. At the far field, a potential flow is assumed with uniform free-stream velocity $\mathbf{U}_\infty = (1, 0)$. A typical computational grid of size 101×101 is shown in Figure 4. We employ a uniform grid spacing along the

DOI: 10.1002/fld

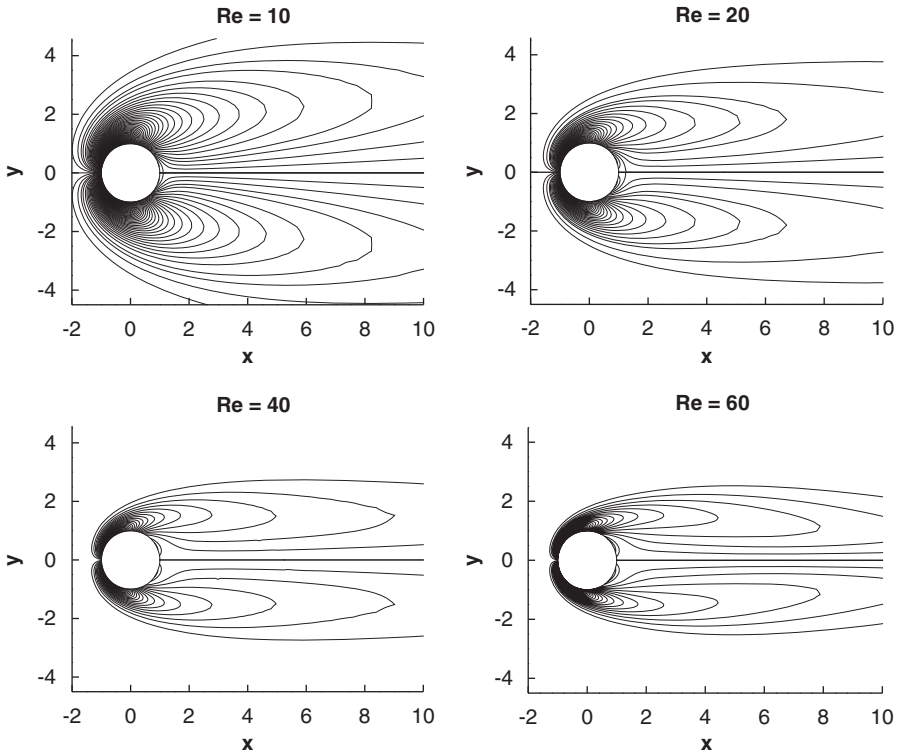

Figure 6. Steady-state vorticity contours for $Re = 10, 20, 40$ and 60 for the motion past a circular cylinder problem.

θ-direction and a nonuniform grid spacing in the r-direction with clustering around the surface of the cylinder using the following functions:

$$\theta_j = \frac{2\pi}{j_{\max}} \quad \text{and} \quad r_i = \exp\left(\frac{\lambda \pi i}{i_{\max}}\right)$$

Here, the parameter λ determines the outer radius of the computational domain. The continuity conditions at $\theta = 0$ and $\theta = 2\pi$ are taken as the boundary conditions along those two lines.

We now derive the boundary conditions for stream function and vorticity. On the solid surface $r = R_0$, $u = v = \psi = 0$. In the far stream $r = R_\infty$, velocity becomes uniform and equal to U_∞ as $r \to \infty$. In terms of stream function, this condition is expressed as $\psi \to U_0 r \sin\theta$ as $r \to \infty$.

For vorticity, the far-stream condition is given by $\omega = 0$ at $r = R_\infty$. On the solid surface $r = R_0$, however, vorticity is not zero. Making use of the fact that $\psi = 0$, $\partial\psi/\partial r = 0$ on $r = R_0$, we arrive at $\omega = -\partial^2\psi/\partial r^2$ thereat. We proceed to obtain a compact approximation of the vorticity on the solid boundary as follows:

$$-v_{0,j} = \left(\frac{\partial \psi}{\partial r}\right)_{0,j} = \delta^+ \psi_{0,j} - \frac{r_f}{2}\left(\frac{\partial^2 \psi}{\partial r^2}\right)_{0,j} - \frac{r_f^2}{6}\left(\frac{\partial^3 \psi}{\partial r^3}\right)_{0,j} + O(r_f^3)$$

DOI: 10.1002/fld

so that we get the finite difference approximation as

$$0=\frac{\psi_{1,j}}{r_f}-\frac{r_f}{2}\left(-\omega_{0,j}\right)-\frac{r_f^2}{6}\left(-\left(\frac{\partial\omega}{\partial r}\right)_{0,j}\right)$$

$$0=\frac{\psi_{1,j}}{r_f}+\frac{r_f}{2}\omega_{0,j}+\frac{r_f^2}{6}\left(\frac{\omega_{1,j}-\omega_{0,j}}{r_f}\right)$$

yielding

$$2\omega_{0,j}+\omega_{1,j}=-\frac{6}{r_f^2}\psi_{1,j} \tag{23}$$

We present steady-state results for this flow for Reynolds numbers $Re=10, 20, 40$ and 60 in Figures 5–7 and Tables II–IV. Simulation for higher Reynolds number was not considered because earlier experimental and numerical studies [29, 30] indicated that the flow no longer remains steady for Re's beyond 60. Therefore, we present flow profiles for Reynolds numbers up to 60 only,

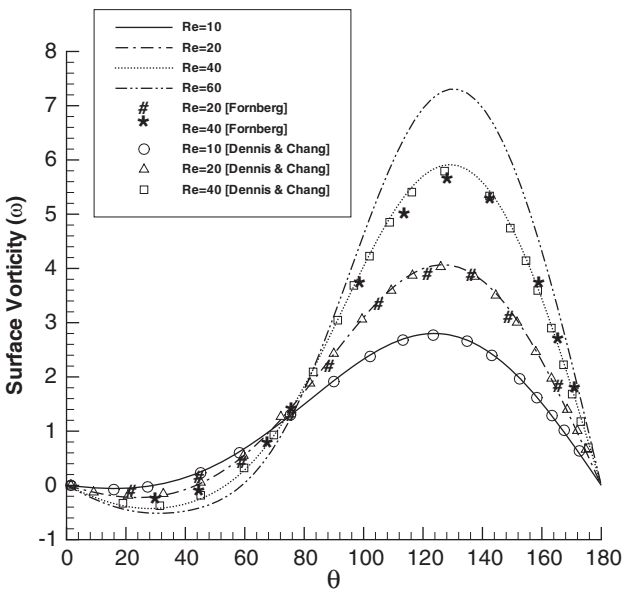

Figure 7. Comparison of vorticities on the cylinder surface for different Res with the results of References [29, 30] for the motion past a circular cylinder problem.

Table II. Problem 2: effect of grid size on wake lengths and separation angles.

	$Re=20$			$Re=40$		
Grid	75	101	151	75	101	151
θ_s	42.9248	43.2756	43.4224	51.3012	51.5342	51.7018
L	1.8331	1.8276	1.8226	4.4135	4.3988	4.3921

DOI: 10.1002/fld

Table III. Problem 2: effect of far-field boundary on the wake lengths and separation angles.

	$Re=20$			$Re=40$		
R_∞	35.03	60.14	75.17	35.03	60.14	75.17
θ_s	43.6248	43.2156	42.9248	51.9612	51.6342	51.3012
L	1.8177	1.8253	1.8331	4.4044	4.4101	4.4135

Table IV. Problem 2: comparison of the wake lengths and separation angles for different Reynolds numbers.

	Re	Reference [29]	Reference [31]	Reference [32]	Reference [30]	Reference [33]	Reference [16]	Reference [34]	Present
L	20	1.88	1.87	1.87	1.82	1.842	1.77	1.92	1.8331
	40	4.69	4.65	4.27	4.48	4.49	4.21	4.51	4.4135
θ_s	20	43.7	—	—	42.9	42.96	41.3277	42.79	42.9248
	40	53.8	—	—	51.5	52.84	51.0249	52.84	51.3012
C_D	20	2.045	2.0027	—	2.001	2.152	2.0597	2.111	2.0193
	40	1.522	1.5359	—	1.498	1.499	1.5308	1.574	1.5145

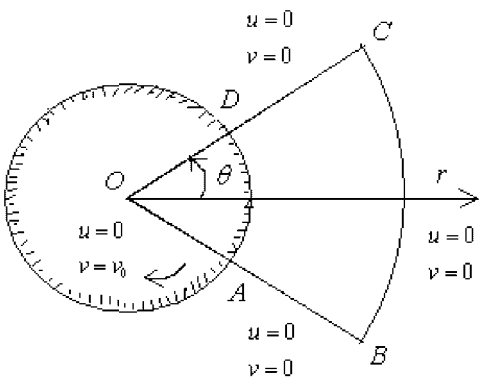

Figure 8. Schematic diagram of the driven polar cavity problem.

more so for $Re=20$ and $Re=40$, for which experimental and numerical results [16, 29–35] exist in plenty.

In Figure 5, we exhibit the streamlines from $Re=10$ to 60. In all the cases, two symmetrical, stationary circulating eddies develop behind the cylinder. With increase in Re values, one can see the increase in the sizes of the vortices. The corresponding vorticity contours for the same range of Reynolds numbers are shown in Figure 6.

It is worth mentioning that though several studies [29, 30, 36] have presented the so-called steady-state results for this flow at $Re=60$, many experimental and numerical results have shown conclusively that eventually asymmetry sets in and the flow becomes unsteady for this Reynolds number [37–43]. Therefore, the results presented here for $Re=60$ may be termed as the simulated converged solution of the N–S equations governing the flow.

We also compute the wake length L: the distance between the rear most point of the cylinder to the end of the wake and the angle of separation θ_s. These parameters are then compared to verify the grid independence and dependence of the computed solution on the assumed far field. In

DOI: 10.1002/fld

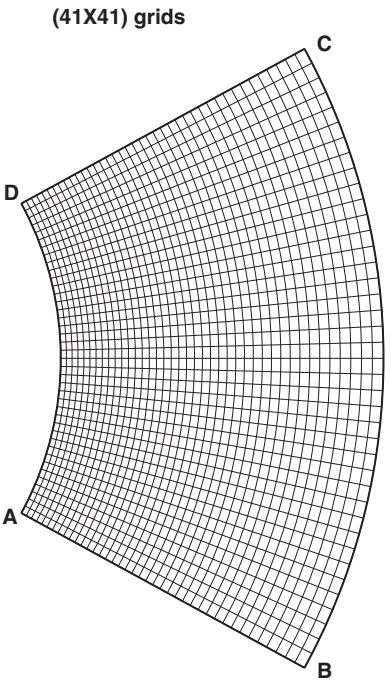

Figure 9. A typical 41×41 nonuniform grid for the driven polar cavity problem.

Table II, we present these parameters on grid sizes ranging from 75×75 to 151×151 and Table III shows the variation of the same parameters for far-field boundaries located at R_∞s ranging from 35.03 to 75.17. Here, the grid size has been fixed at 75×75. From these tables, it is clear that a grid of size 101×101 and a far field given by $R_\infty = 75$ are enough for accurate resolution of the flow. In Table IV, we present our computed L, θ_s and the drag coefficient C_D with those obtained by [16, 29–31, 33, 34]. We also compare the vorticities along the surface of the cylinder for the range of Reynolds numbers considered here with those of References [29, 30] in Figure 7. In all the cases, excellent comparison with the established numerical results is obtained, both qualitatively and quantitatively.

4.3. Test problem 3: driven polar cavity flow

Finally, to validate our proposed HOC scheme, we apply it to solve the driven polar cavity problem. This flow is also governed by the N–S equations (19)–(21). This problem was first studied both experimentally as well as numerically by Fuchs and Tillmark [44]. A schematic diagram of the problem is shown in Figure 8. The region *ABCD* is the domain of the problem. The inner circle *DA* is moving with an angular clock-wise velocity $v = v_0 = 1$, which drives the flow. All the other boundary walls are fixed. Here, u and v are the radial and tangential velocities, respectively; the Reynolds number, Re, is given by $v_0 R_0 / \nu$, where $OD = OA = R_0$ is the radius of the inner circle, v_0 is the surface velocity of the rotating cylinder and ν is the kinematic viscosity of the fluid. No slip boundary conditions are applied on the solid walls. Thus boundary conditions for u and v are

DOI: 10.1002/fld

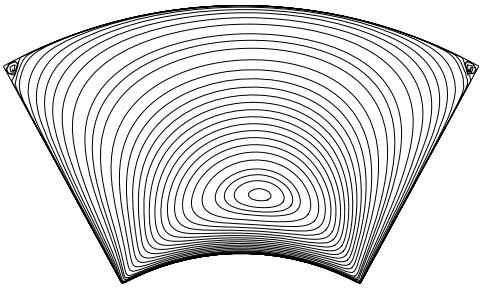

(a)

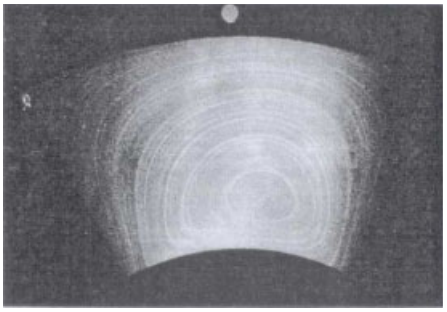

(b)

Figure 10. Steady-state streamlines for the driven polar cavity problem for $Re=55$: (a) numerical and (b) experimental [44].

given by: $u=0, v=1$ on $\widehat{DA}$ and $u=v=0$ on the other three walls. Using the normal velocity boundary conditions, we can get $\psi=0$ on all the boundary walls. Making use of the fact that

$$\frac{\partial^2\psi}{\partial r^2}+\frac{1}{r}\frac{\partial\psi}{\partial r}=-\omega, \quad \psi=0 \quad \text{and} \quad v=-\frac{\partial\psi}{\partial r}=1$$

along the boundary $\widehat{DA}$, we obtain a third-order accurate approximation of ω as

$$\Rightarrow \omega_{0,j}+\frac{\omega_{1,j}}{2}=-\frac{3}{h_0}\left(1+\frac{\psi_{1,j}}{h_0}-\frac{h_0}{2r_0}+\frac{h_0^2}{6r_0^2}\right) \tag{24}$$

as in problem 2, where $h_0=(r_1-r_0)$. In a similar way, one can approximate the vorticities along the other three boundaries as: along $\widehat{AB}$

$$\omega_{i,0}+\frac{\omega_{i,1}}{2}=\frac{3}{r_i^2\Delta\theta_0^2}\psi_{i,1} \tag{25}$$

along $\widehat{BC}$

$$\omega_{n-1,j}+\frac{\omega_{n-2,j}}{2}=\frac{3}{h_{n-2}^2}\psi_{n-2,j} \tag{26}$$

DOI: 10.1002/fld

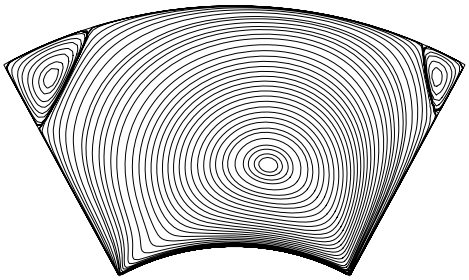

(a)

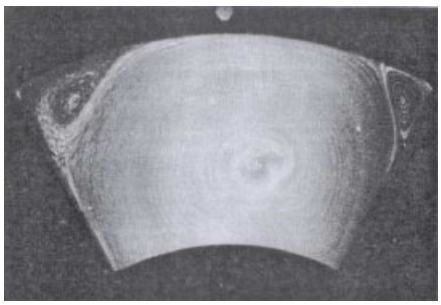

(b)

Figure 11. Steady-state streamlines for the driven polar cavity problem for $Re=350$: (a) numerical and (b) experimental [44].

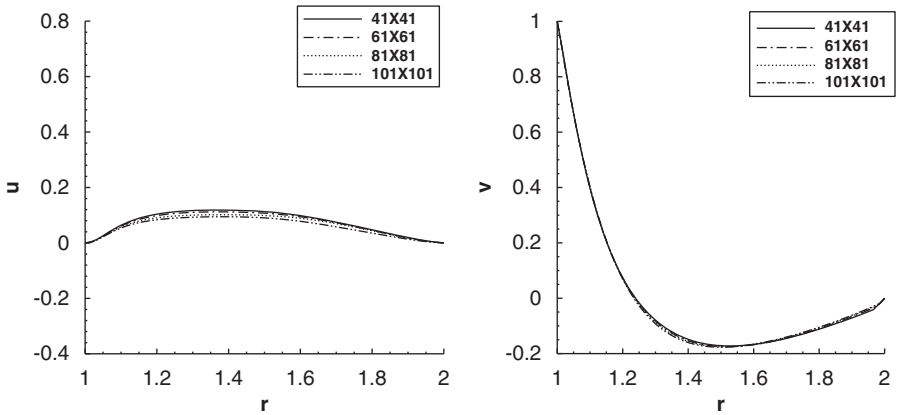

Figure 12. The u- and v-velocity profiles on different grid sizes for the driven polar cavity flow problem along $\theta=0$ for $Re=55$.

along $\widehat{CD}$

$$\omega_{i,m-1}+\frac{\omega_{i,m-2}}{2}=-\frac{3}{r_i^2\Delta\theta_{m-2}^2}\psi_{i,m-2} \tag{27}$$

DOI: 10.1002/fld

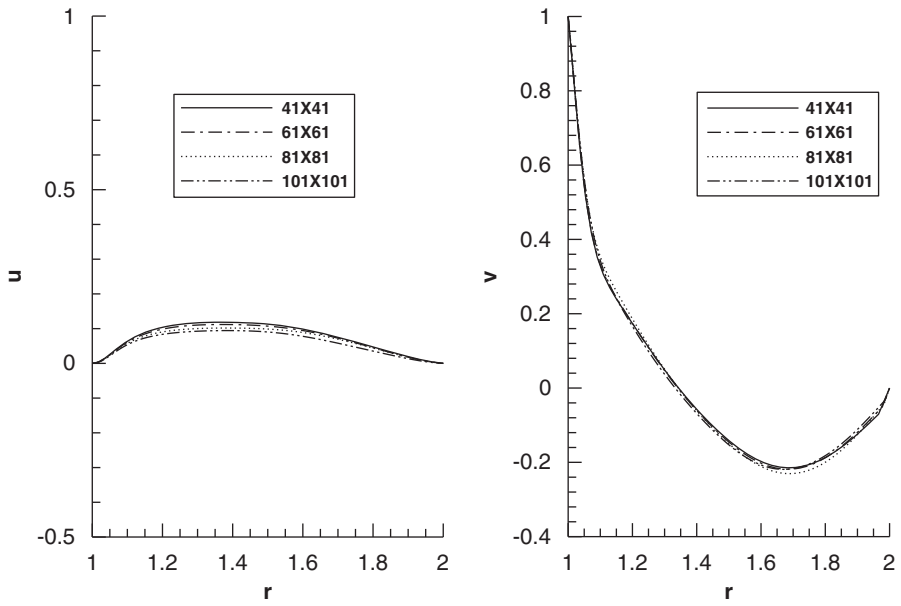

Figure 13. The u- and v-velocity profiles on different grid sizes for the driven polar cavity flow problem along $\theta=0$ for $Re=350$.

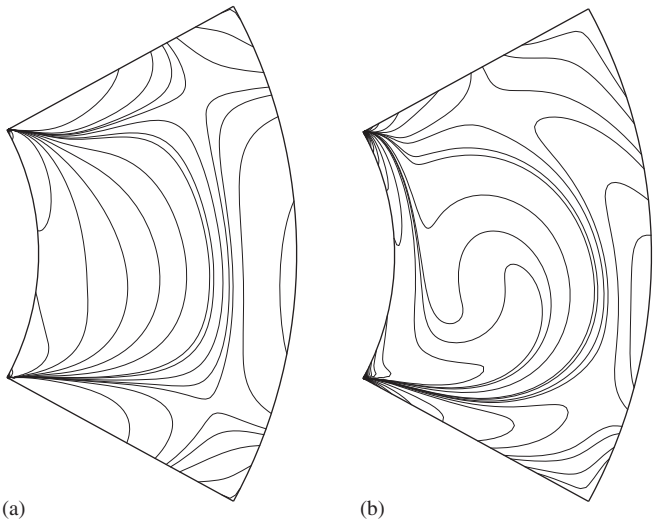

Figure 14. Vorticity contours for (a) $Re=55$ and (b) 350 for the driven polar cavity problem.

where $h_{n-2}=r_{n-1}-r_{n-2}, \Delta\theta_0=\theta_1-\theta_0, \Delta\theta_{n-2}=\theta_{m-1}-\theta_{m-2}$ with $n-1$ and $m-1$ denoting the maximum index along the r and θ-directions, respectively. In their work, Lee and Tsuei [45] observed that the large solution errors propagate near the rotating boundary. Therefore,

DOI: 10.1002/fld

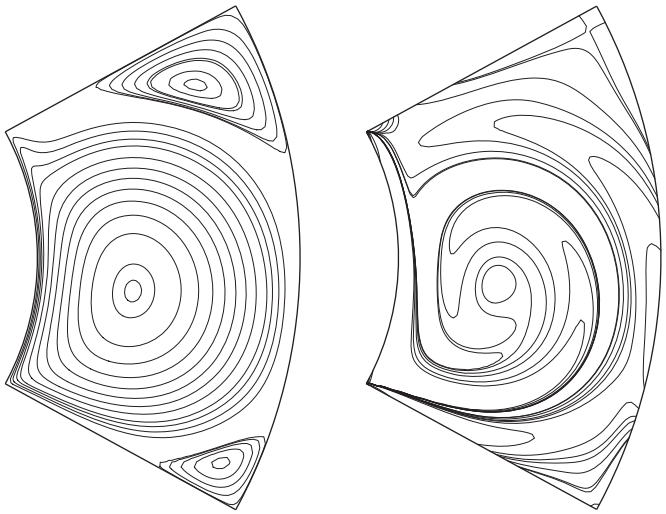

Figure 15. The (a) streamlines and (b) vorticity contours for $Re = 1000$ for the driven polar cavity problem.

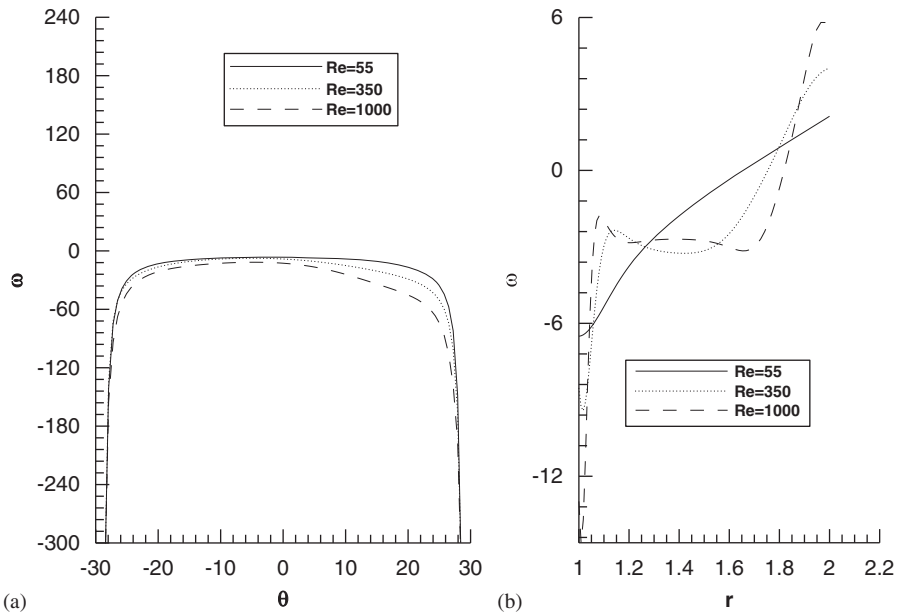

Figure 16. Vorticity (a) along the rotating wall and (b) along the radial line $\theta = 0$ for the driven polar cavity problem.

DOI: 10.1002/fld

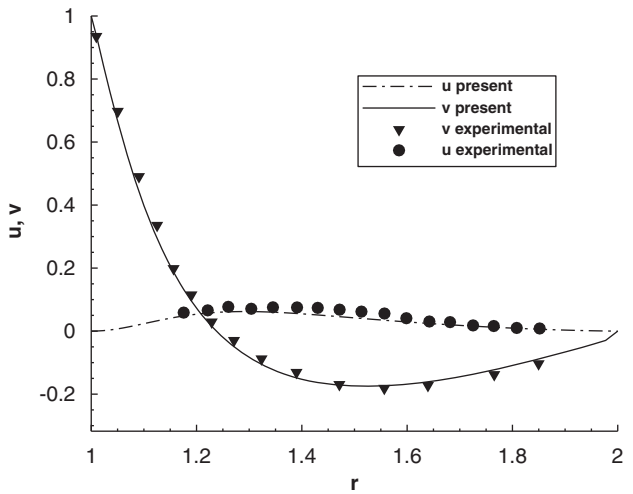

Figure 17. Comparison between experimental and present numerical u and v results for $Re=55$ along the radial line $\theta=0$.

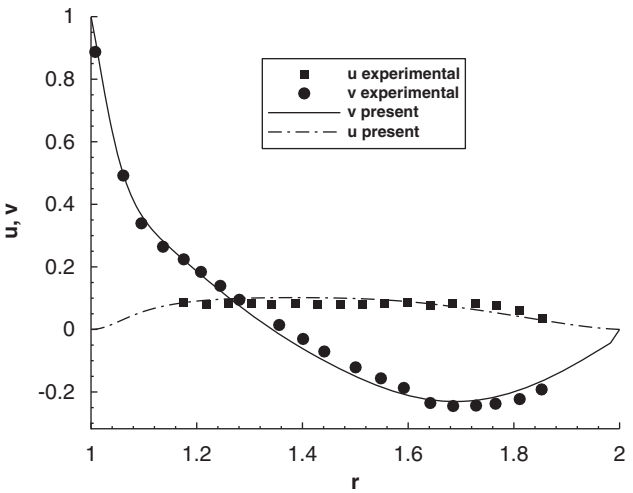

Figure 18. Comparison between experimental and present numerical u and v results for $Re=350$ along the radial line $\theta=0$.

we cluster the region in the vicinity of the rotating boundary using the same stretching functions used in problem 2; Figure 9 shows a typical 41×41 nonuniform mesh used for this problem.

We present our computed solutions in Figures 10–21 and Table V. In Figure 10, we present streamlines obtained from our numerical simulation on an 81×81 grid side by side with the one obtained from the experimental results of [44] for $Re=55$. The corresponding comparison for $Re=350$ on a same grid size is shown in Figure 11.

DOI: 10.1002/fld

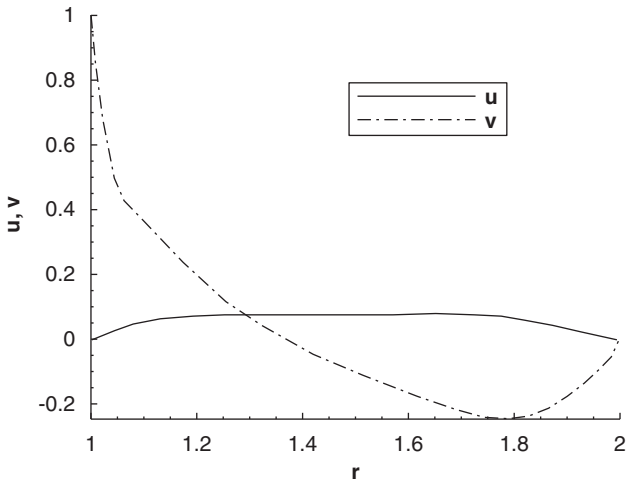

Figure 19. u and v plots for $Re=1000$ along the radial line $\theta=0$.

In Figures 12 and 13 we, respectively, present the u- and v-velocity profiles along $\theta=0$ on four different grid sizes $41\times41, 61\times61, 81\times81$ and 101×101 for Re's 55 and 350, respectively. From these figures, it is clear that a 61×61 grid is enough to achieve grid-independence for $Re=55$ while we needed an 81×81 grid for $Re=350$.

Figure 14 shows the vorticity contours for $Re=55$ and $Re=350$. In Figure 15, we show the streamlines and vorticity contours for $Re=1000$; our streamline patterns are very similar to those in Reference [44]. In Figures 16(a) and (b), we exhibit the variation of the vorticity along the rotating wall $\widehat{DA}$ and the radial line $\theta=0$, respectively.

In Figure 17, we present the u- and v-velocities along the radial line $\theta=0$ obtained through our computation on an 81×81 grid for $Re=55$ along with the experimental results of [44]. Similar comparison for $Re=350$ is presented in Figure 18. In both the cases, we achieve an excellent agreement between the numerical and experimental results. It may be mentioned that in [44], although the numerical results were close to the experimental ones for lower Re's, their high Re results, even on the finest grids were not adequate enough to match the experimental results. The reason for this could be the use of lower-order (first or at most second order) approximation of the derivative terms. As no data are available for Reynolds number 1000 in literature, we present our computed u- and v-velocity profiles along the radial line $\theta=0$ in Figure 19.

In Table V, we present the optimal successive under-relaxation parameter γ for the inner BiCGStab(2) iterations used in our computations for $Re=55$ and 350 on three different grids along with the CPU times. For the outer iterations, the γ value was fixed at 0.650 for both ψ and ω after a series of experiments. It is heartening to note that on a relatively finer 81×81 grid, for $Re=350$, steady-state solution is obtained in less than 1.5 min.

We also exhibit the convergence history in Figures 20 and 21, which provides a clear picture of the fall of the inner BiCGStab(2) iteration number and the infinity norm against the outer iteration number till steady state. In Figure 20, we present the convergence history of the inner BiCGStab(2) iteration against the outer iterations for ω and ψ for $Re=55$ and 350; likewise in Figure 21, we present the fall of the infinity norm for the same flow variables and

DOI: 10.1002/fld

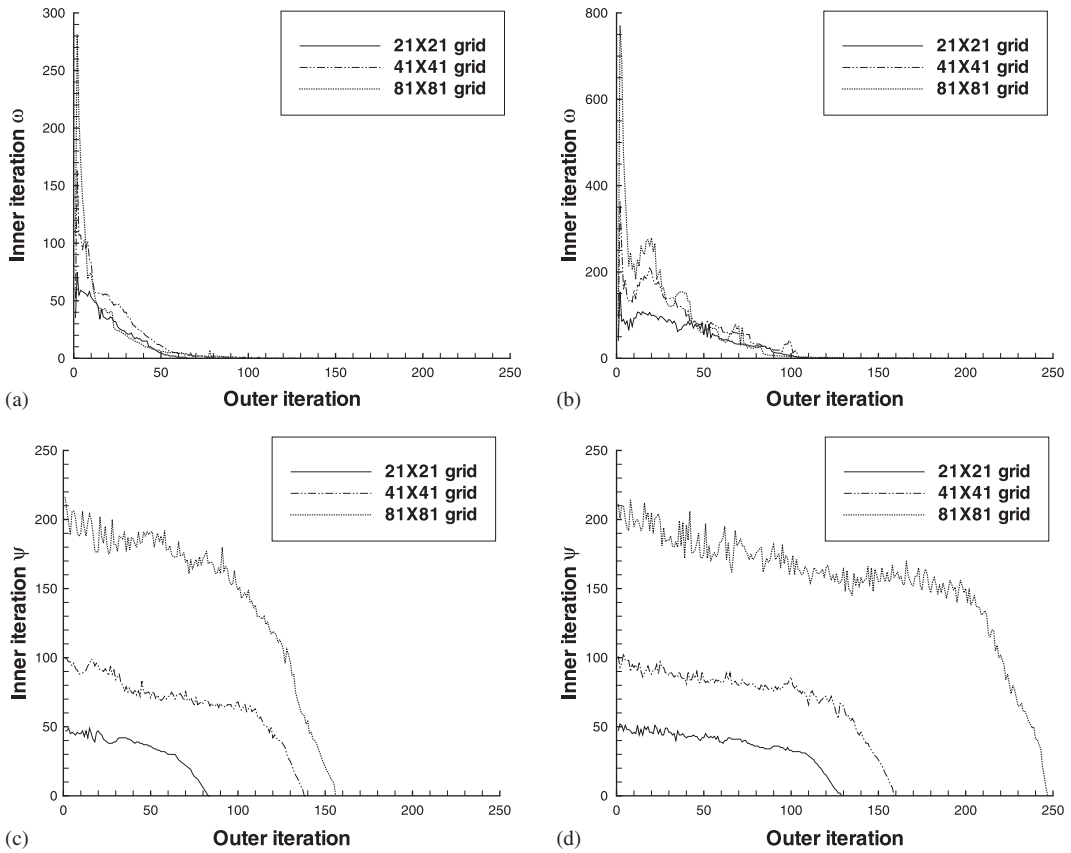

Figure 20. Convergence history: outer iteration versus inner iteration of (a) ω for $Re=55$; (b) ω for $Re=350$; (c) ψ for $Re=55$; and (d) ψ for $Re=350$.

Reynolds numbers. These figures clearly indicate that the convergence pattern is smooth in all the cases.

5. CONCLUSION

In this paper, we extend a recently developed HOC scheme for the steady-state convection diffusion equations on nonuniform Cartesian grids to cylindrical polar grids; further extension of the scheme to general curvilinear coordinate system is straightforward. To bring out different aspects of the scheme, we first apply this new approach to a diffusion equation having analytical solution, then to the motion past an impulsively started circular cylinder and finally to the driven polar cavity problem. In the process, we also demonstrate the fourth-order spatial accuracy of our scheme. In the first problem, Dirichlet boundary conditions are used and for the other two, compact higher-order approximations have been developed and successfully implemented for the Neumann boundary conditions. The robustness of the scheme is illustrated by its applicability to the last two fluid flow

DOI: 10.1002/fld

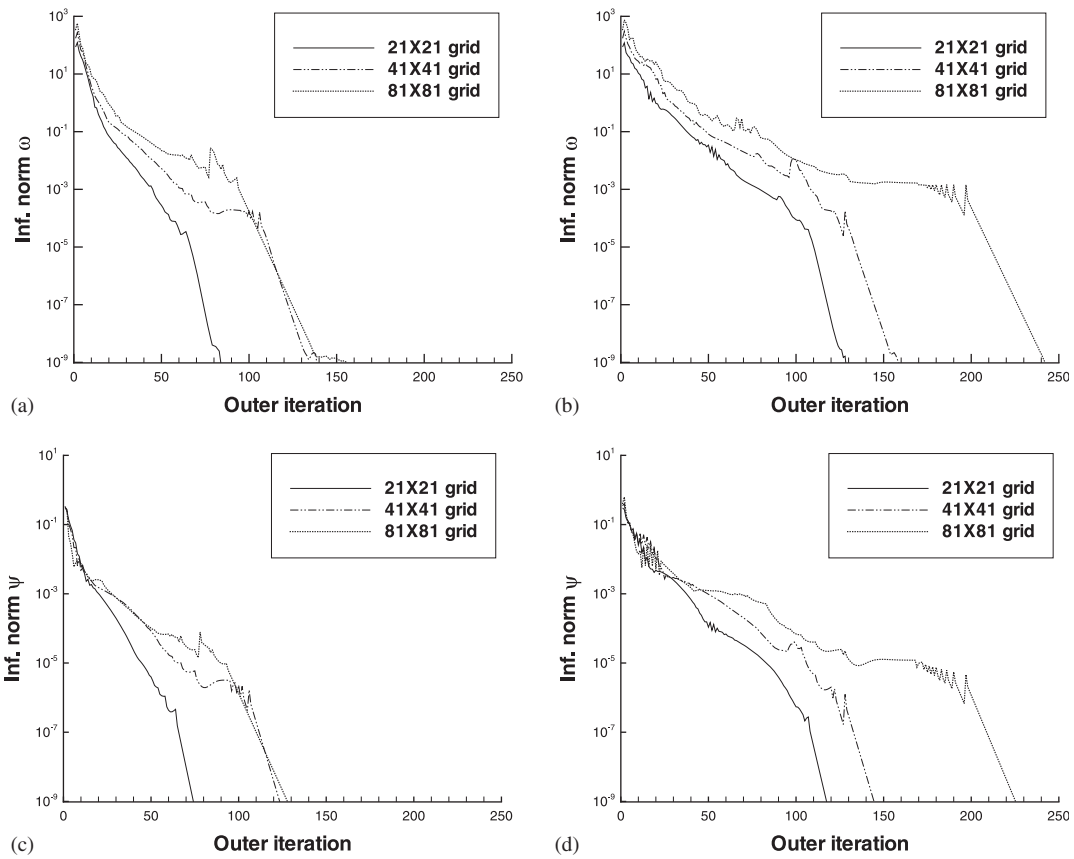

Figure 21. Convergence history: outer iteration versus infinity norm of (a) ω for $Re=55$; (b) ω for $Re=350$; (c) ψ for $Re=55$; and (d) ψ for $Re=350$.

Table V. Problem 3: comparison of CPU times and under-relaxation parameter γ for the BiCGStab inner ieratios on different grids for $Re=55$ and 350.

Re	Grid size	γ for ω	γ for ψ	CPU time (in seconds)
55	21×21	0.305	0.650	0.408
	41×41	0.205	0.500	4.368
	81×81	0.150	0.350	40.011
350	21×21	0.325	0.600	0.944
	41×41	0.225	0.500	7.516
	81×81	0.175	0.375	81.237

problems of varying physical complexities and their accurate computations. In addition, the use of the hybrid biconjugate gradient stabilized algorithm for solving the algebraic systems arising at every outer iteration step makes the solution procedure computationally efficient in capturing the steady-state solutions. The results obtained in all the test cases on relatively coarser grids are in

DOI: 10.1002/fld

excellent agreement with analytical, experimental and established numerical results, underlying the high accuracy of the scheme. As our scheme has the added advantage of being applicable to general orthogonal curvilinear coordinate system, it has tremendous potential for efficient computation of more complex problems of incompressible viscous flows. Currently we are working on the extension of this formulation to transient flows.

APPENDIX A: DETAILS OF THE FINITE DIFFERENCE OPERATORS

The expressions for the finite difference operators appearing in the various equations in Section 2 are as follows:

$$\delta_r \phi_{i,j} = \frac{\phi_{i+1,j} - \phi_{i-1,j}}{2\Delta r}$$

$$\delta_\theta \phi_{i,j} = \frac{\phi_{i,j+1} - \phi_{i,j-1}}{2\Delta \theta}$$

$$\delta_r^2 \phi_{i,j} = \frac{1}{\Delta r}\left\{\frac{\phi_{i+1,j}}{r_f} - \left(\frac{1}{r_f} + \frac{1}{r_b}\right)\phi_{i,j} + \frac{\phi_{i-1,j}}{r_b}\right\}$$

$$\delta_\theta^2 \phi_{i,j} = \frac{1}{\Delta \theta}\left\{\frac{\phi_{i,j+1}}{\theta_f} - \left(\frac{1}{\theta_f} + \frac{1}{\theta_b}\right)\phi_{i,j} + \frac{\phi_{i,j-1}}{\theta_b}\right\}$$

$$\delta_r^2 \delta_\theta \phi_{i,j} = \frac{1}{2\Delta r \Delta \theta}\left\{\frac{1}{r_f}(\phi_{i+1,j+1} - \phi_{i+1,j-1}) - \left(\frac{1}{r_f} + \frac{1}{r_b}\right)(\phi_{i,j+1} - \phi_{i,j-1}) + \frac{1}{r_b}(\phi_{i-1,j+1} - \phi_{i-1,j-1})\right\}$$

$$\delta_r \delta_\theta^2 \phi_{i,j} = \frac{1}{2\Delta r \Delta \theta}\left\{\frac{1}{\theta_f}(\phi_{i+1,j+1} - \phi_{i-1,j+1}) - \left(\frac{1}{\theta_f} + \frac{1}{\theta_b}\right)(\phi_{i+1,j} - \phi_{i-1,j}) + \frac{1}{\theta_b}(\phi_{i+1,j-1} - \phi_{i-1,j-1})\right\}$$

$$\delta_r^2 \delta_\theta^2 \phi_{i,j} = \frac{1}{\Delta r \Delta \theta}\left\{\frac{\phi_{i+1,j+1}}{r_f \theta_f} + \frac{\phi_{i-1,j+1}}{r_b \theta_f} - \left(\frac{1}{r_f \theta_f} + \frac{1}{r_b \theta_f}\right)\phi_{i,j+1} - \left(\frac{1}{r_f \theta_f} + \frac{1}{r_f \theta_b}\right)\phi_{i+1,j} + \left(\frac{1}{r_f \theta_f} + \frac{1}{r_f \theta_b} + \frac{1}{r_b \theta_f} + \frac{1}{r_b \theta_b}\right)\phi_{i,j} - \left(\frac{1}{r_f \theta_b} + \frac{1}{r_b \theta_b}\right)\phi_{i,j-1} - \left(\frac{1}{r_b \theta_f} + \frac{1}{r_b \theta_b}\right)\phi_{i-1,j} + \frac{\phi_{i+1,j-1}}{r_f \theta_b} + \frac{\phi_{i-1,j-1}}{r_b \theta_b}\right\}$$

$$\delta_r \delta_\theta \phi_{i,j} = \frac{1}{4\Delta r \Delta \theta}\{\phi_{i+1,j+1} - \phi_{i+1,j-1} - \phi_{i-1,j+1} + \phi_{i-1,j-1}\}$$

DOI: 10.1002/fld

Here, $r_f=(r_{i+1}-r_i)$, $r_b=(r_i-r_{i-1})$, $\theta_f=(\theta_{j+1}-\theta_j)$, $\theta_b=(\theta_j-\theta_{j-1})$, $\Delta r=(r_f+r_b)/2$ and $\Delta\theta=(\theta_f+\theta_b)/2$ as defined in Section 2.

REFERENCES

1. Kalita JC, Dalal DC, Dass AK. A class of higher order compact schemes for the unsteady two-dimensional convection–diffusion equations with variable convection coefficients. *International Journal for Numerical Methods in Fluids* 2002; **38**:1111–1131.
2. Kalita JC, Dass AK, Dalal DC. A transformation-free HOC scheme for steady state convection–diffusion on non-uniform grids. *International Journal for Numerical Methods in Fluids* 2004; **44**:33–53.
3. Gupta MM, Manohar RM, Stephenson JH. A single cell high order scheme for the convection–diffusion equation with variable coefficients. *International Journal for Numerical Methods in Fluids* 1984; **4**:641–651.
4. Gupta MM. High accuracy solutions of incompressible Navier–Stokes equations. *Journal of Computational Physics* 1991; **93**:343–359.
5. MacKinnon RJ, Carey. Analysis of material interface discontinuities and super convergent fluxes in finite difference theory. *Journal of Computational Physics* 1988; **75**:151–167.
6. Mackinnon RJ, Johnson RW. Differential equation based representation of truncation errors for accurate numerical solution. *International Journal for Numerical Methods in Fluids* 1991; **13**:739–757.
7. Spotz WF, Carey GF. High-order compact scheme for the steady stream-function vorticity equations. *International Journal for Numerical Methods in Engineering* 1995; **38**:3497–3512.
8. Lele SK. Compact finite difference schemes with spectral like resolution. *Journal of Computational Physics* 1992; **103**:16–42.
9. Strikwerda JC. High-order accurate schemes for incompressible viscous flow. *International Journal for Numerical Methods in Fluids* 1997; **24**:715–734.
10. Li M, Tang T, Fornberg B. A compact fourth order finite difference scheme for the steady incompressible Navier–Stokes equations. *International Journal for Numerical Methods in Fluids* 1995; **20**:1137–1151.
11. Kalita JC, Chhabra P. An improved (9,5) higher order compact scheme for the transient two-dimensional convection–diffusion equation. *International Journal for Numerical Methods in Fluids* 2006; **51**:703–717.
12. Spotz WF, Carey GF. Formulation and experiments with high-order compact schemes for nonuniform grids. *International Journal for Numerical Methods of Heat and Fluid Flow* 1998; **8**(3):288–303.
13. Pandit SK, Kalita JC, Dalal DC. A fourth-order accurate compact scheme for the solution of steady Navier–Stokes equation on non-uniform grids. *Computers and Fluids* 2008; **37**(2):121–134.
14. Pandit SK, Kalita JC, Dalal DC. A transient higher order compact scheme for incompressible viscous flows on geometries beyond rectangular. *Journal of Computational Physics* 2008; **225**(1):1100–1124.
15. Gupta MM. A fourth order Poisson solver. *Journal of Computational Physics* 1984; **55**:166–172.
16. Sanyasiraju YVSS, Manjula V. Flow past an impulsively started circular cylinder using a higher-order semicompact scheme. *Physical Review E* 2005; **72**(016709):1–10.
17. Zhang J, Lixin GE, Gupta MM. Fourth order compact difference scheme for 3D convection–diffusion equation with boundary layers on nonuniform grids. *Neural, Parallel and Scientific Computations* 2000; **8**:373–392.
18. Mohseni K, Colonius T. Numerical treatment of polar coordinate singularities. *Journal of Computational Physics* 2000; **157**:787–795.
19. Lai MC. A simple compact fourth-order Poisson solver on polar geometry. *Journal of Computational Physics* 2002; **182**:337–345.
20. Borges L, Daripa P. A fast parallel algorithm for Poisson solvers on a disk. *Journal of Computational Physics* 2001; **169**:151–192.
21. Iyenger SRK, Manohar R. High order finite difference methods for heat equation in polar cylindrical coordinates. *Journal of Computational Physics* 1988; **77**:425–438.
22. Jain MK, Jain RK, Krishna M. A fourth order difference scheme for quasilinear Poisson equation in polar coordinates. *Communications in Numerical Methods in Engineering* 1994; **10**:791–797.
23. Lai MC, Wang WC. Fast direct solvers for Poisson equation on 2D polar and spherical geometries. *Numerical Methods for Partial Differential Equations* 2002; **18**:56–68.
24. Zhuang Y, Sun XH. A high order fast direct solver for singular Poisson equations. *Journal of Computational Physics* 2001; **171**:79–94.
25. Muralidhar K, Sundararajan T (eds). In *Computational Fluid Flow and Heat Transfer*: *IIT Kanpur Series of Advanced Texts*. Narosa Publishing House: New Delhi, 2003; 187–192.

DOI: 10.1002/fld

26. Constantinescu GS, Lele SK. A highly accurate technique for the treatment of flow equations at the polar axis in cylindrical coordinates using series expansions. *Journal of Computational Physics* 2002; **183**:165–186.
27. Sleijpen GLG, van der Vorst HA. Hybrid bi-conjugate gradient methods for CFD problems. In *Computational Fluid Dynamics Review*, Hafez M, Oshima K (eds). Wiley: Chichester, 1995; 457–476.
28. Kelley CT. *Iterative Methods for Linear and Nonlinear Equations*. SIAM: Philadelphia, 1995.
29. Dennis SCR, Chang GZ. Numerical solution for study flow past a circular cylinder at Reynolds numbers up to 100. *Journal of Fluid Mechanics* 1970; **42**:471–489.
30. Fornberg B. A numerical study of steady viscous flow past a circular cylinder. *Journal of Fluid Mechanics* 1980; **98**:819–855.
31. Takami H, Keller HB. Steady two-dimensional viscous flow of an incompressible fluid past a circular cylinder. *Physics of Fluids* 1969; **12**(Suppl. II):11–51.
32. Loc TP. Numerical analysis of unsteady secondary vortices generated by an impulsively started circular cylinder. *Journal of Fluid Mechanics* 1980; **100**:111–128.
33. He X, Doolen G. Lattice Boltzmann method on curvilinear coordinates system: flow around a circular cylinder. *Journal of Computational Physics* 1997; **134**:306–315.
34. Niu XD, Chew YT, Shu C. Simulation of flows arround an impulsively started circular cylinder by Taylor series expansion and least squares-based lattice Boltzmann method. *Journal of Computational Physics* 2003; **188**:176–193.
35. Koumoutsakos PK, Leonard A. High-resolution simulations of the flow around an impulsively started cylinder using vortex methods. *Journal of Fluid Mechanics* 1995; **296**:1–38.
36. Fornberg B. Steady viscous flow past a circular cylinder up to Reynolds number 600. *Journal of Computational Physics* 1985; **61**:297–320.
37. Batchelor GK. *An Introduction to Fluid Dynamics*. Cambridge University Press: Cambridge, 2005.
38. Panton RL. *Incompressible Flow*. Wiley: New York, 1984.
39. Schlichting H, Gersten K. *Boundary Layer Theory* (8th Revised, Enlarged edn). Springer: New Delhi, 2004.
40. Zdravkovich MM. *Flow Around Circular Cylinders*; *Vol. 1*: *Fundamentals*. Oxford University Press: New York, 1997.
41. Mittal S, Raghuvanshi A. Control of vortex shedding behind circular cylinder for flows at low Reynolds numbers. *International Journal for Numerical Methods in Fluids* 2001; **35**:421–447.
42. Tritton DJ. Experiments on the flow past a circular cylinder at low Reynolds numbers. *Journal of Fluid Mechanics* 1959; **6**:547–567.
43. Williamson CHK. Oblique and parallel modes of vortex shedding in the wake of a circular cylinder at low Reynolds numbers. *Journal of Fluid Mechanics* 1989; **206**:579–627.
44. Fuchs L, Tillmark N. Numerical and experimental study of driven flow in a polar cavity. *International Journal for Numerical Methods in Fluids* 1985; **5**:311–329.
45. Lee D, Tsuei YM. A hybrid adaptive gridding procedure for recirculating fluid flow problems. *Journal of Computational Physics* 1993; **108**:122–141.

DOI: 10.1002/fld